Journal name
000(00):1–13

DOI:doi number
http://mms.sagepub.com

Simulating the aerodynamic characteristics of the Land Speed Record vehicle, BLOODHOUND SSC

B. Evans *
College of Engineering, Swansea University, UK

C. Rose
College of Engineering, Swansea University, UK

Abstract

This paper describes the application of a parallel finite volume compressible Navier–Stokes CFD solver to the complex aerodynamic problem of a land–based supersonic vehicle, the BLOODHOUND SSC. This is a complex aerodynamic problem due to the supersonic rolling ground, rotating wheels and shock waves in close proximity to the ground. The CFD system is used to develop a mature vehicle design from initial concept stage and the major aerodynamic design changes are identified. The paper's focus, however, is on the predicted aerodynamic behaviour of the finalised (frozen) design which is currently being manufactured. The paper presents a summary of the databank of predicted aerodynamic behaviour that will be used as the benchmark for vehicle testing and CFD validation throughout 2014 and 2015 in an attempt to achieve a Land Speed Record (LSR) of 1,000 mph (approximately Mach 1.3). The CFD predictions indicate that the current design has a benign lift distribution across the whole Mach range of interest and sufficiently low drag coefficient to achieve this objective. It also indicates that the fin has been sized appropriately to achieve the static margin requirements for directional stability. The paper concludes by presenting the impact of feeding the CFD predictions detailed into the overall vehicle performance model along with recommendations for further CFD study.

Keywords

CFD, aerodynamic design, BLOODHOUND SSC

1. Introduction

The first Land Speed Record (LSR) was set by Frenchman Gaston de Chasseloup-Laubat at Achères in France in 1898. This first LSR was set at the modest speed of 39 mph in an electric powered car. The Record has since been broken around sixty times with the current (supersonic) Record of 763.035 mph (Mach 1.02) being set by Andy Green in THRUST SSC (SuperSonic Car) at the Black Rock Desert, Nevada in 1997. A significant feature of the THRUST SSC project was the manner in which computational fluid dynamics (CFD) was applied to guide the aerodynamic design process (1; 2; 3).

* Corresponding author; e-mail: b.j.evans@swansea.ac.uk

Fig. 1. Artist's impression of the config12 BLOODHOUND SSC geometry including corporate livery

The BLOODHOUND project was launched in October 2008 with a primary engineering objective of designing, building and running a car to achieve a new LSR of 1,000 mph. This engineering objective is coupled with an educational objective to promote science, technology, engineering and mathematics (STEM) to school children in the UK and beyond via the BLOODHOUND education programme. Clearly, the aerodynamic challenges associated with developing a land–based vehicle capable of safely achieving speeds of up to 1,000 mph (approximately Mach 1.3) are great, particularly at supersonic speeds. Drag minimisation and vertical aerodynamic force control are of paramount importance for a safe record attempt on the constrained distance of 12 miles available at the record attempt site in Hakskeen Pan, South Africa. Again, CFD has been chosen as the primary tool to guide the aerodynamic design of the vehicle. The CFD system used in this study was the Swansea University FLITE3D system (4; 5). This is a classical cell–vertex, finit–volume method, with stabilisation and discontinuity capturing, implemented on hybrid, unstructured meshes (6; 7).

This paper will briefly describe the CFD process used to analyse such a complex aerodynamic problem but its focus will be on the predicted aerodynamic behaviour of the final, frozen, design (known as config12) of BLOODHOUND SSC. It will outline both on and off-design aerodynamic characteristics of the vehicle and consider the impact of differing engine conditions and directional stability. An artist's impression of the config12 BLOODHOUND SSC geometry is shown in Figure 1.

2. Governing Equations

The unsteady compressible Navier–Stokes equations are expressed, over a fixed 3D domain Ω, with closed surface Γ, in the integral form

$$\int_\Omega \frac{\partial \vec{U}}{\partial t}\,\mathrm{d}\vec{x} + \int_\Gamma \vec{F}_j n_j\,\mathrm{d}\vec{x} = \int_\Gamma \vec{G}_j n_j\,\mathrm{d}\vec{x} \qquad \text{for } j = 1, 2, 3 \tag{1}$$

where, relative to an (x_1, x_2, x_3) Cartesian coordinate system, $\vec{n} = (n_1, n_2, n_3)$ is the unit outward normal vector to Γ and the summation convention is employed. The unknown vector, of conservative variables, is expressed as

$$\vec{U} = \begin{bmatrix} \rho \\ \rho u_1 \\ \rho u_2 \\ \rho u_3 \\ \rho \epsilon \end{bmatrix} \tag{2}$$

where ρ is the fluid density, $\vec{u} = (u_1, u_2, u_3)$ is the fluid velocity vector and ϵ is the specific total energy of the fluid. The inviscid and viscous flux vectors are written as

$$\vec{F}_j = \begin{bmatrix} \rho u_j \\ \rho u_1 u_j + p\delta_{1j} \\ \rho u_2 u_j + p\delta_{2j} \\ \rho u_3 u_j + p\delta_{3j} \\ u_j(\rho\epsilon + p) \end{bmatrix} \qquad \vec{G}_j = \begin{bmatrix} 0 \\ \tau_{1j} \\ \tau_{2j} \\ \tau_{3j} \\ u_k\tau_{kj} - q_j \end{bmatrix} \tag{3}$$

Here, p denotes the pressure in the fluid, δ_{ij} is the Kronecker delta and

$$\tau_{ij} = -\frac{2}{3}\mu\frac{\partial u_k}{\partial x_k}\delta_{ij} + \mu\left(\frac{\partial u_i}{\partial x_j} + \frac{\partial u_j}{\partial x_i}\right) \tag{4}$$

is the deviatoric stress tensor, where μ is the dynamic viscosity of the fluid. The quantity $q_j = -k(\partial T/\partial x_j)$ is the heat flux in the direction x_j, where k and T denote the thermal conductivity and the absolute temperature of the fluid respectively. The viscosity is assumed to vary with temperature according to Sutherland's law and the Prandtl number is assumed to be constant and equal to 0.72. The state equations for the fluid are assumed to be those appropriate for a calorically perfect gas.

3. Solution Procedure

3.1. Hybrid Unstructured Mesh Generation

The computational domain is represented by an unstructured hybrid mesh. The process of mesh generation begins with the discretization of the domain boundary into a set of triangular or quadrilateral elements that satisfy the requirements of a user–specified mesh control function. This function defines the distribution of the mesh spacing, stretching and direction of stretching (6) using a background mesh and a distribution of sources (7). For the domain mesh, tetrahedral elements are generated first in the boundary layer regions, using the advancing layer method (8). The remainder of the computational domain is then filled with tetrahedral elements using a Delaunay method with point creation (9). Hybrid unstructured meshes are constructed by merging appropriate tetrahedral elements in the boundary layer regions.

3.2. Spatial Discretisation

The governing equations are discretised using a cell vertex finite volume method, which requires the identification of a dual mesh. For primal tetrahedral cells, the median dual is employed in which the surface of each dual mesh cell is constructed as an assembly of triangular facets, Γ_I^K. These facets are formed by connecting edge midpoints, element centroids and face centroids in the primal mesh, and are assembled in such a way that only one primal mesh vertex is contained within each dual mesh cell. When hybrid meshes are employed, the method for constructing the median dual has to be modified in order to ensure that no node lies outside its corresponding control volume.

In the cell vertex finite volume approach, the unknowns are located at the primal mesh vertices and equation (1) is satisfied over each dual mesh cell in turn. To perform the numerical integration of the fluxes, a set of coefficients is calculated for each edge using the dual mesh segment associated with the edge. For a typical internal node I, edge coefficients, C_j^{IJ}, are defined, for the edge in the mesh joining node I to node J, as

$$C_j^{IJ} = \sum_{K \in \Gamma_{IJ}} A_{\Gamma_I^K} n_j^{\Gamma_I^K} \tag{5}$$

where $A_{\Gamma_I^K}$ is the area of facet Γ_I^K and $n_j^{\Gamma_I^K}$ is the outward unit normal vector to the facet. The numerical integration of the fluxes over the dual mesh segment associated with an edge is performed by assuming the flux to be constant, and equal to its approximated value at the midpoint of the edge, i.e. a form of mid point quadrature is employed. The integral of the inviscid flux, over the control volume surface corresponding to primary mesh vertex I, is then approximated as

$$\int_{\partial\Omega_I} \mathbf{F}_j n_j d\mathbf{x} \approx \sum_{J\in\Lambda_I} \frac{C_j^{IJ}}{2}\left(\mathbf{F}_j^I + \mathbf{F}_j^J\right) \tag{6}$$

where Λ_I denotes the set of vertices directly connected to node I. A similar approximation can be developed for the viscous flux terms once the nodal gradients of the appropriate flow variables have been determined. These discretisations will require appropriate modification for vertices I that are located on the computational boundary.

The second order diffusion term is calculated using a compact stencil (5), where the gradient along the edges are evaluated by means of the compact finite difference scheme. The resulting discretisation requires stabilisation before practical flow simulations can be attempted. Here, this is achieved by replacing the physical flux function by the HLLC (10; 11) consistent numerical flux function.

3.3. Time Discretization

The time derivative in equation (1) is evaluated using the three level, second order accurate backward difference approximation

$$\left.\frac{\partial\vec{U}}{\partial t}\right|^n \approx \frac{1}{\Delta t}\left(\frac{3}{2}\vec{U}^n - 2\vec{U}^{n-1} + \frac{1}{2}\vec{U}^{n-2}\right) \tag{7}$$

where the superscript n denotes an evaluation at time $t = t_n$ and the time interval between t_{n-2} and t_{n-1} and between t_{n-1} and t_n is denoted by Δt. The resulting equation system is solved, at each time level $t = t_n$, by an explicit three stage Runge–Kutta approach with local pseudo–time stepping to explicitly relax the solution towards steady–state. Steady state convergence is assumed when the density residual has decreased by 3 orders of magnitude.

4. Turbulence Modelling

The density–weighted Favre time–averaging procedure is applied to equation (1) to produce the compressible Reynolds–averaged Navier Stokes (RANS) equations. This process smooths the instantaneous turbulent fluctuations in the flow field, while still allowing the capture of the time dependency in the time scales of interest, and results in the appearance of the Favre–averaged Reynolds stress tensor

$$\tau_{ij}^R = -\overline{\rho u_i' u_j'} \tag{8}$$

where the overbar denotes the Favre average. These unknown Reynolds stresses can be associated with the computed mean flow quantities by using a suitable turbulence model. Use of the Boussinesq hypothesis results in the linear relationship

$$\tau_{ij}^R = \mu_t\left(\frac{\partial U_i}{\partial x_j} + \frac{\partial U_j}{\partial x_i} - \frac{2}{3}\frac{\partial U_k}{\partial x_k}\delta_{ij}\right) - \frac{2}{3}\rho k\delta_{ij} \tag{9}$$

where μ_t is the eddy viscosity (12) and k is the turbulent kinetic energy. The eddy viscosity depends on the velocity and length scale, ℓ, of the turbulent eddies, i.e. $\mu_t \sim k^{1/2}\ell$. A complete two equation model is adopted, in which two additional transport equations are solved and the non–local and history effects on μ_t are considered. The $k-\omega$ model is popular, due to its good performance for boundary layer flows subjected to adverse pressure gradients. The original $k-\omega$ model exhibits a free-stream dependency of ω, which is generally not present in the $k-\epsilon$ model (12). Menter (13; 14) combined the advantages of both models by means of blending functions, that permit the switching from $k-\omega$, close to a wall, to

$k-\epsilon$, when approaching the edge of a boundary layer. A further improvement is a modification to the eddy viscosity, based on the idea of the Johnson–King model, which establishes that the transport of the main turbulent shear stresses is crucial in the simulations of strong adverse pressure gradient flows. This is the approach advocated in the Menter shear stress transport (SST) model (13; 14).

5. Initial and Boundary Conditions

To complete the specification of the problem, boundary conditions must be defined over the entire boundary of the computational domain. In the case of simulating the full BLOODHOUND SSC vehicle aerodynamics, this includes farfield boundaries, viscous walls, jet engine / rocket exhausts and jet intake (15).

5.1. Inflow and Outflow Boundaries

A characteristic treatment (16) is employed at simple inflow and outflow boundaries to determine the number, and type, of conditions that require specification at any given point.

5.2. Viscous Walls

For viscous flow, the no slip condition

$$\vec{u} = \vec{u}^w \tag{10}$$

is strongly applied, where $\vec{u}^w$ is a specified wall velocity. When simulating a vehicle with rotating wheels, the vector $\vec{u}^w$, at a point with position vector $\vec{r}$ on the wheel relative to a user–specified position on the axis of rotation, is computed as

$$\vec{u}^w = \vec{\omega} \times \vec{d} \tag{11}$$

where, as illustrated in Figure 2(a),

$$\vec{d} = \vec{r} - \frac{(\vec{\omega}.\vec{r})}{|\vec{\omega}|}\vec{\omega} \tag{12}$$

is the position vector of the point relative to the centre of the wheel and $\vec{\omega}$ is the user–specified wheel rotation vector. All the simulations are performed with the vehicle at rest and this requires that the ground moves with the speed of the vehicle but in the opposite direction. The combined effect of the rotating wheel and rolling ground velocity boundary condition field is illustrated, for a single wheel, in Figure 2(b). This boundary condition definition for the ground plane assumes that it behaves as an impervious surface at the same temperature as the local flow. The validity of this assumption will be explored during early vehicle testing. Note that the wheel intersects with the rolling ground surface assuming a penetration depth of 15mm. This assumption is based on observations of wheel–ground interaction behaviour during the Thrust SSC LSR project (1). This is another assumption that will require validation during vehicle testing.

5.3. Jet engine / Rocket exhaust

Supersonic inflow conditions (density, velocity and pressure), provided by the engine and rocket manufacturers, are applied strongly at the engine and rocket exhausts.

5.4. Jet Engine Inflow

The internal flow within BLOODHOUND's EJ200 jet engine is not modelled. The internal portion of the engine is considered to lie outside of the computational domain. This implies that an outflow boundary condition is required at the engine's compressor face. The most useful descriptor of the demand placed on an aerodynamic flow by a jet engine face

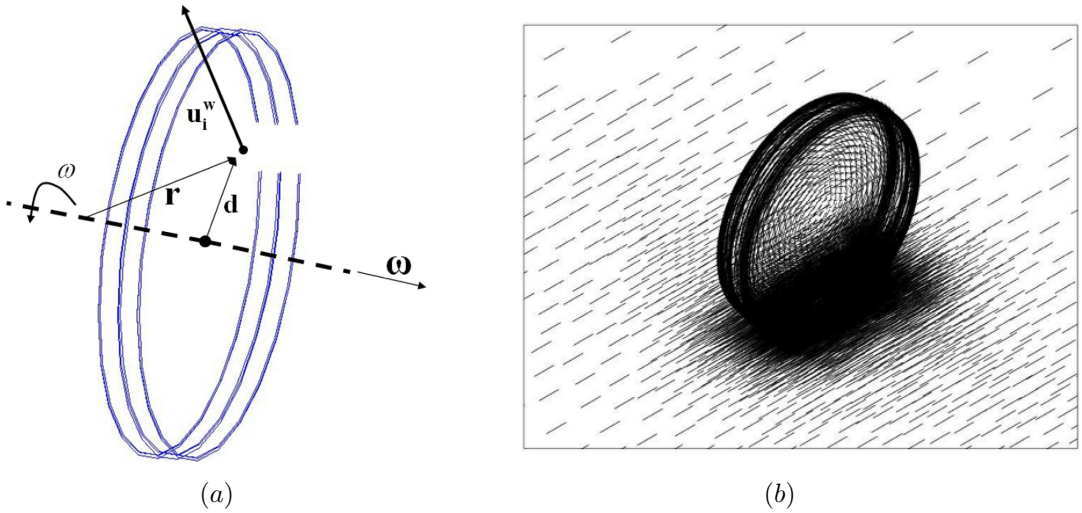

(a) (b)

Fig. 2. Simulation of a rotating wheel, showing:(a) interpretation of the boundary condition implementation; (b) the velocity vector field on the rotating wheel and on the rolling ground

is the specification of a non–dimensional mass flow function (15; 17) relating the mass flow rate, total temperature and total pressure experienced at the compressor face. This mass flow function depends on the throttle setting of the engine and the free–stream Mach number. This information is provided by the engine manufacturer. At each timestep the mass flow function requirement is satisfied using an iterative technique based on locally modifying the velocity vector field at the engine face by 'stretching' (or compressing) the vector field in the direction perpendicular to the plane as necessary.

5.5. Turbulence Equations

The results produced by a steady simulation, starting from free-stream conditions across the entire computational domain, are used to provide an initial condition for the transient simulations. The application of the boundary conditions for the basic flow parameters, such as velocity, density and total energy, is classical (4).

In the Menter SST model, the turbulent kinetic energy, k, is assigned a zero value at the wall. The specific dissipation rate, ω, does not possess a natural boundary condition at the wall. However, based on the asymptotic solution given by Wilcox (12), the value

$$\omega_o = \frac{6\nu_w}{\beta y_w^2 \mathrm{Re}_\infty} \tag{13}$$

is prescribed, where ν_w is the laminar kinematic viscosity at the wall, $\beta = 3/40$, y_w is the local normal distance to the first off–wall point and Re_L is the local Reynolds number. At inflow and outflow boundaries, the values $k_\infty = 1 \times 10^{-6}$ and $\omega_\infty = 5$ are imposed (18). At a symmetry boundary, where the normal velocity component is zero, the turbulent eddy viscosity is set to zero. For simulations involving engines, the interior of the engine is assumed to lie outside the computational domain and free-stream values for the turbulence variables are prescribed at the engine inlet and outlet faces.

6. Improving computational performance

The computational performance of the solution algorithm is improved by the use of parallel processing in order to ensure a reasonable turnaround time for each simulation. The parallel implementation involves the subdivision of the original domain into a number of sub–domains, such that each sub–domain comprises of a distinct set of mesh edges, along with the corresponding nodes that form the ends of each edge. This has the effect that nodes at the interface between two

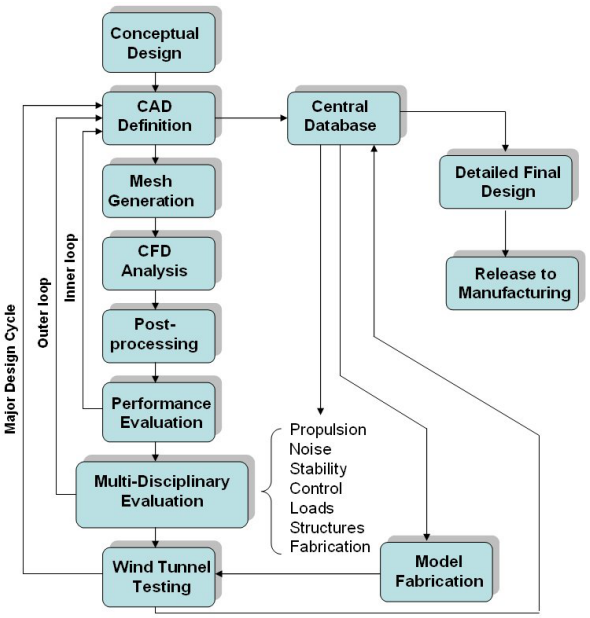

Fig. 3. A typical multi–disciplinary aerospace design cycle

sub–domains are duplicated. The solver is executed in parallel utilising one process per sub–domain. At the start of a time step, the interface nodes obtain contributions from the interface edges. These partially updated contributions are transmitted to the corresponding interface nodes in the neighbouring sub–domains. A loop over the interior edges is followed by the receiving of the interface node contributions and the subsequent updating of all interior nodal values. This procedure is implemented in such a way as to allow computation and communication to be performed concurrently, where permitted by the parallel computer's hardware (15).

In order to optimise performance, and achieve scalability on a large number of processors, the chosen domain decomposition strategy must produce sub–domains of a balanced size and with a minimum number of cut edges. This ensures that each processor has to perform an equal amount of work and that the amount of communication between processors is minimised. This has been achieved by utilising the METIS family of partitioning algorithms (19). Each sub–domain node list is renumbered to maximise the use of cache memory in order to further improve computational performance.

7. The BLOODHOUND SSC Aerodynamic Problem

In the past three decades, CFD has revolutionised the way in which the aerospace industry tackles problems of aerodynamic design. In particular, unstructured mesh methods now allow grids on complex three–dimensional geometries to be generated, in a matter of hours, that might once have taken several months using multiblock techniques. In light of this, CFD has become an integral part of the typical aerodynamic design cycle, as indicated in Figure 3. This flow chart indicates the emphasis now placed on CFD within the inner and outer design loops. On the BLOODHOUND project, for practicality, financial restrictions and time constraints, the Major Design Cycle loop is essentially the actual vehicle runway and desert testing. This is where validation of the CFD modelling used in the inner loops will take place. It may well be the case that vehicle testing will require significant re–design and entering back into the inner design loops (note that, at the time of writing, the BLOODHOUND is in the build phase with anticipated build completion by mid–2014 followed by vehicle testing throughout late 2014 and 2015).

The design process for the 1,000 mph BLOODHOUND vehicle started with the conceptual configuration shown in Figure 4. The design iterations taking the external shape of the vehicle from the conceptual design through to a realisable

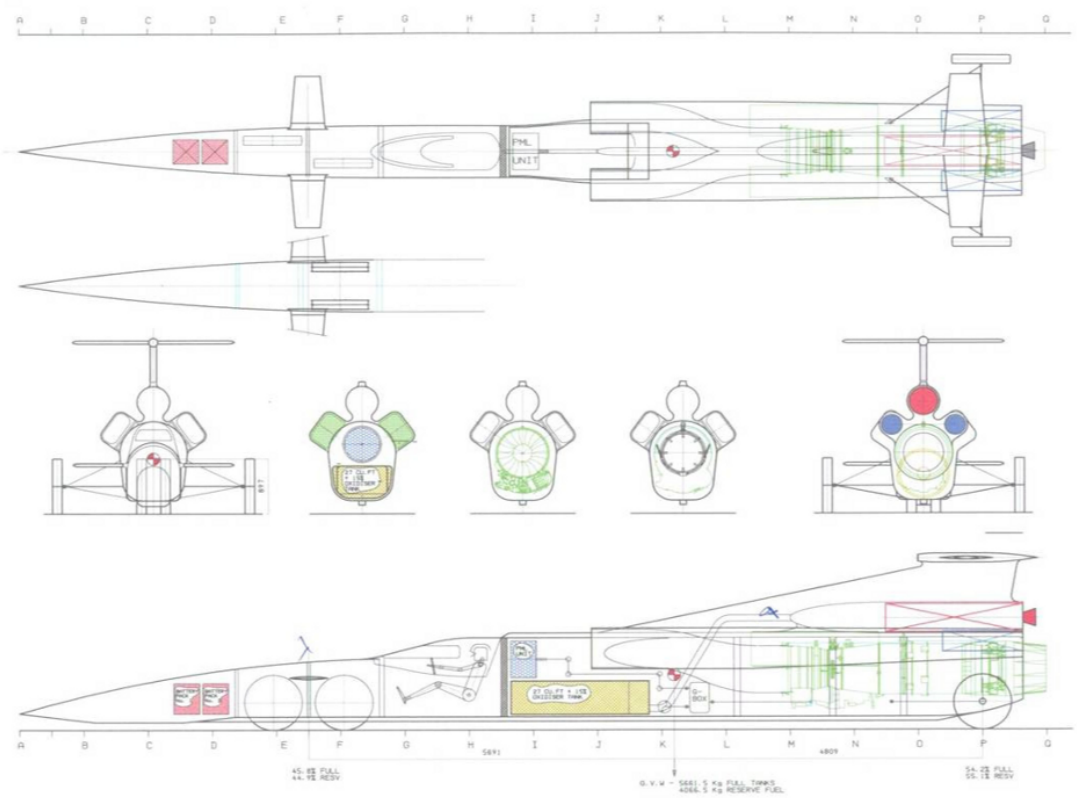

Fig. 4. Drawing illustrating the initial concept layout of BLOODHOUND SSC

engineering solution is shown in Figure 5. Each configuration (config) is a product of the outer loop of the design cycle in Figure 3 (20). The external vehicle shape iterations, feeding into the wider engineering design cycle, were driven primarily by CFD simulations of the full vehicle. Typically, each full aerodynamic vehicle design iteration, i.e., the inner loop in Figure 3 required 2 months for meshing, and sufficient simulation and post–processing to guide the designers on to the subsequent configuration (15). This is due to the large number of steady state solutions required for each new configuration over a range of Mach numbers at design and off–design conditions (e.g. in yaw / crosswind).

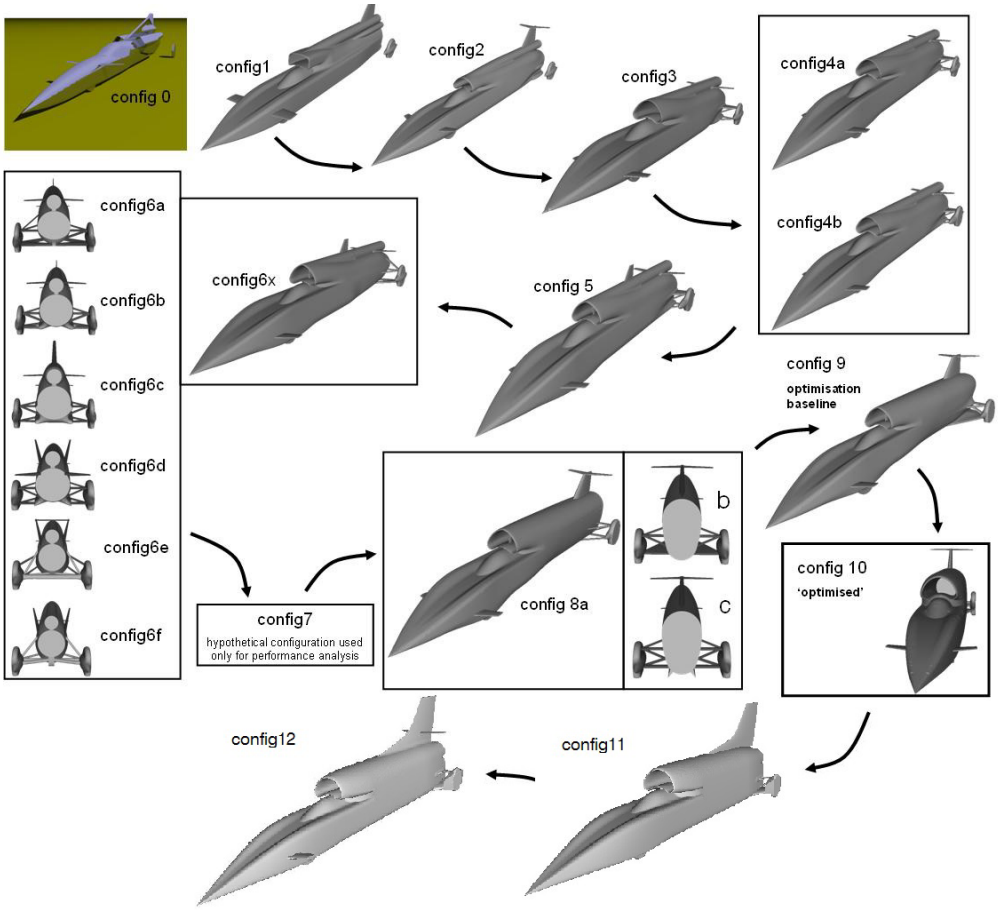

Fig. 5. BLOODHOUND design iterations from config0 (2007) to config12 (2012)

The major design changes that have taken place during the design cycles as a result of aerodynamic modelling are as follows (15; 22):-

1) Between config0 and config1 a transition was made from a twin (bifurcated) jet intake to a single jet intake design. This change was made to improve the 'quality' of the flow at the jet compressor face across the Mach range. The front wheels also moved from a staggered configuration to a symmetric configuration (15).

2) Between config1 and config4 the positioning of the rear winglets and vertical fin was varied and the rear suspension was designed and included in the CFD model.

3) Between config4 and config6 the rear wheel suspension geometry was varied along with body shaping as a result of internal packaging constraints. The size and area distribution of the jet intake was also varied.

4) config7 existed only as a hypothetically perfect vehicle from an aerodynamic performance point of view. This hypothetical data was used in the overall vehicle performance model as a baseline case to give an indication of criteria such as the required track length for vehicle testing.

5) config8 introduced the rear 'delta fairing' (22) for supersonic lift minimisation at the rear of the vehicle.

6) Between config9 and config12 a series of parametric optimisation studies (22) were carried out along with an increase in fin size to achieve the directional static margin target.

8. Results: Simulated Aerodynamic Performance

The 12 stage design process detailed in Figure 5 guided the vehicle's external shape from the initial config0 geometry to the finalised (frozen) config12 geometry over a period of approximately 5 years. This section details the aerodynamic characteristics of the final config12 vehicle shape at both design conditions and off-design conditions.

The complex geometry of the frozen config12 design resulted in a surface mesh of 222,433 nodes and 457,616 triangular surface elements. The hybrid unstructured volume mesh contained 61,454,678 cells with approximately $1/3$ of these cells comprising the high resolution boundary layer mesh. Simulations were run on a PC cluster consisting of 32 8–core 2.4GHz Intel processors. A typical simulation would require between 4 and 7 days of clock time to converge the densisity residual by three orders of magnitude.

A series of steady state simulations was used to determine the aerodynamic performance characteristics of the vehicle across a diverse range of conditions. The aerodynamics of the vehicle under acceleration and deceleration was considerd by varying the jet and rocket parameters at inflow and exhaust (the engine throttle will be reduced to idle for deceleration and the rocket switched off). The FLITE3D CFD solver produces aerodynamic force coefficients and moments about a user–defined datum. In the case of the simulations detailed in this paper, the datum was set to the mid–wheelbase position on the ground surface as shown in Figure 6. These were used to construct a data bank of simulated vehicle behaviour. The force and moment coefficients are defined as,

$$C_F = \frac{F}{q_\infty} \tag{14}$$

$$C_M = \frac{M}{q_\infty} \tag{15}$$

where F denotes the total integrated force in a given direction, M represents a total integrated moment about a datum position and q_∞ is the free-stream dynamic pressure

$$q_\infty = \frac{1}{2}\rho_\infty v_\infty^2 \tag{16}$$

where ρ_∞ and v_∞ represent the free-stream density and velocity of the fluid respectively. As a result of these definitions, force and moment coefficients have units m^2 and m^3 respectively.

The longitudinal moment coefficients were used to distribute the total lift coefficient experienced by the vehicle between the front and rear wheel contact patches as shown in Figure 6. Note that the total lift is equal to the sum of the front and rear lift values.

This lift distribution is important in order to determine the reaction forces at the front and rear wheels which feed into the overall vehicle performance model. Similarly, the directional moment coefficient was used to determine the directional (yaw) centre of pressure (CoP) position relative to the datum, and hence, relative to the known centre of gravity (CG) position. The displacement of the CoP relative to the CG ('b' in Figure 6) defines the yaw static margin of the vehicle and hence, its directional stability.

BLOODHOUND SSC is designed to achieve a peak velocity of 1,050 mph during the measured mile whilst remaining in contact with the ground. At these speeds the air pressure acting upon the structure is estimated to peak at over 12 tonnes per square meter. Overall vehicle performance modelling resulted in a target peak supersonic drag coefficient of 1.3 m^2 in order to achieve the target velocity within the 12 track available at the record attempt location, Hakskeen Pan, South Africa.

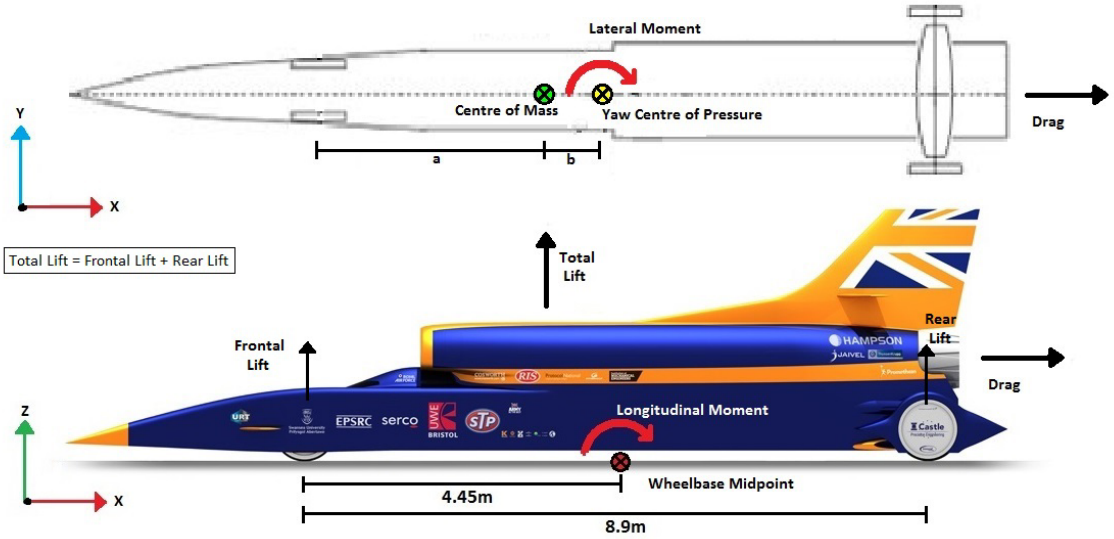

Fig. 6. Drawing illustrating the location of the midpoint and axis of design concept

8.1. Design Conditions: 0° yaw

A series of steady state simulations were performed across the Mach range of interest from $M_\infty = 0.3$ to $M_\infty = 1.5$ at intervals of $M_\infty = 0.1$ in the subsonic and supersonic regions. In the transonic region, transient shock waves exist and dominate the flow characteristics, therefore simulations were performed at intervals of $M_\infty = 0.05$ between $M_\infty = 0.6$ and $M_\infty = 1.0$.

Under design conditions, i.e. yaw$= 0°$, the lateral forces acting on the vehicle should be zero. The non–zero lateral force coefficients (LatF/q), lateral and roll moment coefficients shown in Tables 1 and 2, are due to the inevitable asymmetries in the computational mesh resulting from the unstructured mesh generation process.

Table 1 shows the variation with Mach number of force coefficients (total lift, frontal lift, rear lift, drag, skin friction and lateral force) and moment coefficients (longitudinal, lateral and roll) about the mid–wheel base datum position with the engine boundary conditions set to max throttle conditions i.e. vehicle accelerating. Table 2 shows the variation with Mach number of force coefficients and moment coefficients with the jet engine boundary conditions set to idle and the rocket exhaust condition switched off. The lift and drag coefficient variations with Mach number are shown graphically in Figure 9.

It is evident that the front lift coefficient variation with Mach number is small compared with the rear lift variation with Mach number. The reason for this is clear from Figure 7. The pressure distribution across the front half of the vehicle over both the underside and top of the vehicle varies little. However, at the rear of the vehicle there is a significant shift in the pressure distribution on the underside from suction at $M_\infty = 0.5$ to positive pressures at $M_\infty = 1.3$. This distinct change in flow pattern is driven by the shock waves that are generated due to the rear wheels and suspension system. The result of these shock waves is highlighted in the pressure coefficient plots of Figure 8. As a result of this phenomenon, the total lift steadily increases through the subsonic and transonic regions, becoming positive as the vehicle reaches $M_\infty = 0.9$. The absolute total lift acting on the vehicle peaks at approximately $M_\infty = 1.0$ at $0.273 \times 0.5 \times 1.2 \times 343 \times 343 \approx 19kN$ assuming a free-stream density of $1.2kg/m^3$ and sound speed of $343m/s$.

Table 1 indicates that the maximum drag coefficient is $1.323m^2$ at $M_\infty = 1.1$ but drops back below the supersonic drag coefficient target of $1.3m^2$ by the time the vehicle reaches $M_\infty = 1.2$.

	Mach Number	Lift/q (m^2)	Front Wheel Lift/q (m^2)	Rear Wheel Lift/q (m^2)	Drag/q (m^2)	Skin Friction/q (m^2)	Lateral Force/q (m^2)	Longitudinal Moment/q (m^3)	Lateral Moment/q (m^3)	Roll Moment/q (m^3)
↑	0.30	-1.164	0.038	-1.203	1.081	0.268	0.0107	5.521	-0.0310	0.0108
subsonic	0.40	-0.997	-0.064	-0.933	1.085	0.201	0.0069	3.864	-0.0262	0.0063
	0.50	-0.857	-0.013	-0.844	1.092	0.166	0.0060	3.700	-0.0200	0.0051
↓	0.60	-0.786	-0.058	-0.727	1.098	0.146	0.0055	2.975	-0.0170	0.0050
↑	0.65	-0.646	-0.035	-0.611	1.096	0.136	0.0034	2.564	-0.0125	0.0035
	0.70	-0.591	-0.041	-0.550	1.027	0.132	0.0033	2.264	-0.0101	0.0038
	0.75	-0.437	-0.030	-0.407	1.160	0.132	0.0025	1.678	0.0000	0.0051
transonic	0.80	-0.379	-0.004	-0.375	1.004	0.122	0.0034	1.650	-0.0082	0.0033
	0.85	-0.103	0.030	-0.133	1.086	0.116	0.0054	0.726	-0.0210	0.0050
↓	0.90	0.113	0.042	0.071	1.136	0.112	0.0032	-0.130	-0.0127	0.0024
↑	0.95	0.286	0.094	0.192	1.142	0.108	0.0025	-0.435	-0.0069	0.0022
	1.00	0.273	0.115	0.158	1.254	0.102	0.0008	-0.193	0.0028	0.0001
	1.10	0.122	0.076	0.047	1.323	0.102	0.0039	0.131	-0.0180	0.0004
supersonic	1.20	0.045	0.051	-0.006	1.214	0.088	-0.0006	0.253	-0.0023	-0.0047
	1.30	-0.007	0.037	-0.044	1.107	0.080	0.0003	0.359	-0.0056	-0.0022
	1.40	-0.038	0.030	-0.068	1.016	0.074	0.0006	0.437	-0.0076	-0.0013
↓	1.50	-0.065	0.025	-0.089	0.936	0.070	0.0006	0.507	-0.0056	-0.0007

Table 1. Characteristics for maximum thrust with 0° yaw - Acceleration

	Mach Number	Lift/q (m^2)	Front Wheel Lift/q (m^2)	Rear Wheel Lift/q (m^2)	Drag/q (m^2)	Skin Friction/q (m^2)	Lateral Force/q (m^2)	Longitudinal Moment/q (m^3)	Lateral Moment/q (m^3)	Roll Moment/q (m^3)
↑	0.30	-0.744	-0.066	-0.679	0.336	0.267	0.0013	2.728	0.0023	0.0011
subsonic	0.40	-0.747	-0.135	-0.611	0.421	0.208	0.0038	2.119	-0.0112	0.0036
	0.50	-0.842	-0.125	-0.718	0.620	0.165	0.0053	2.639	-0.0151	0.0051
↓	0.60	-0.781	-0.191	-0.590	0.886	0.152	0.0023	1.779	-0.0061	0.0029
↑	0.65	-0.594	-0.062	-0.532	0.875	0.128	0.0100	2.093	-0.0337	0.0110
	0.70	-0.429	-0.001	-0.428	0.960	0.131	0.0084	1.902	-0.0313	0.0094
	0.75	-0.411	-0.020	-0.390	0.892	0.116	0.0084	1.646	-0.0297	0.0085
transonic	0.80	-0.350	-0.066	-0.284	0.895	0.114	0.0083	0.970	-0.0309	0.0073
	0.85	-0.136	-0.046	-0.090	0.982	0.110	0.0090	0.195	-0.0327	0.0068
↓	0.90	0.154	0.033	0.121	1.069	0.106	0.0089	-0.388	-0.0291	0.0073
↑	0.95	0.247	0.043	0.204	1.199	0.105	0.0078	-0.717	-0.0306	0.0046
	1.00	0.289	0.088	0.201	1.334	0.098	0.0063	-0.502	-0.0119	0.0064
	1.10	0.186	0.066	0.120	1.363	0.088	-0.0003	-0.242	0.0105	0.0013
supersonic	1.20	0.097	0.044	0.052	1.325	0.080	0.0008	-0.036	-0.0085	-0.0047
	1.30	0.039	0.031	0.007	1.276	0.078	0.0008	0.108	-0.0045	-0.0019
	1.40	0.001	0.025	-0.024	1.186	0.073	0.0017	0.218	-0.0082	-0.0001
↓	1.50	-0.092	0.016	-0.108	0.906	0.070	0.0020	0.551	-0.0060	0.0016

Table 2. Characteristics under idle engine conditions with 0° yaw - Deceleration

BLOODHOUND SSC experiences similar lift contributions for idle engine conditions as to operating at maximum thrust. It is obvious that the majority of the lift contribution develops in the supersonic region by the aerodynamic forces acting near the rear of the vehicle. Also, it is clear that the majority of the supersonic drag is pressure drag, with the skin friction drag coefficient actually decreasing with Mach number. This is to be expected since from the point at which shock waves appear, in the transonic region, wave drag dominates.

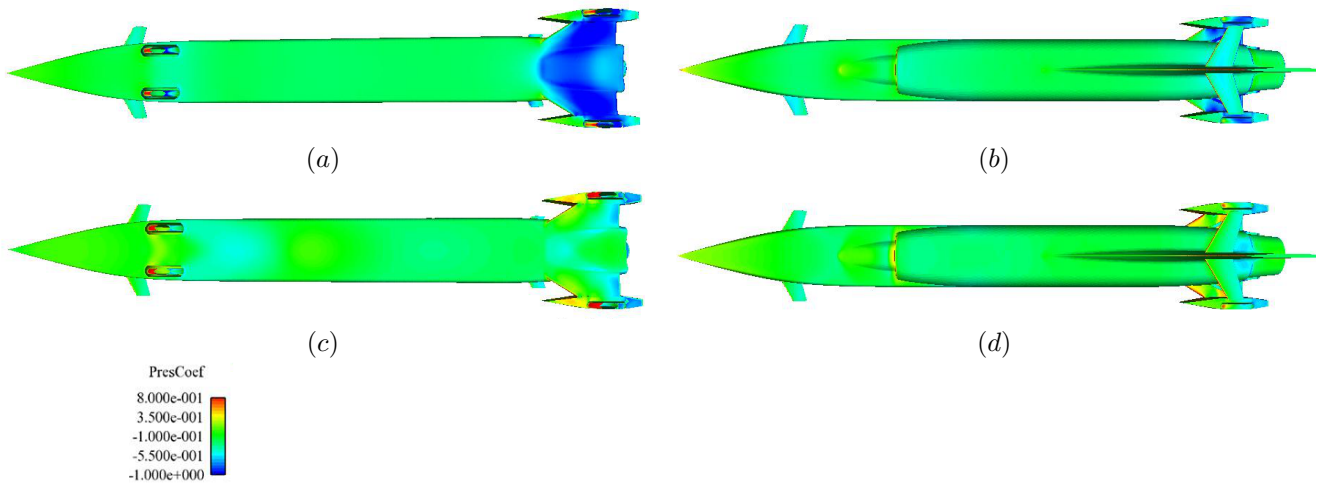

Fig. 7. Pressure coefficient distribution across external surfaces:(a) underside $M_\infty = 0.5$; (b) top $M_\infty = 0.5$; (c) underside $M_\infty = 1.3$; (d) top $M_\infty = 1.3$

8.2. Off-Design: Yaw Stability - 2° Yaw

It is inevitable that due to transient external conditions (wind gusts, track inconsistency etc.) BLOODHOUND SSC will not consistently operate 'on–design' as outlined in the previous section. Therefore a series of simulations of off–design conditions, specifically at small yaw angles i.e. yaw=2°, were performed across the Mach range of interest, at intervals of $M_\infty = 0.05$ during the transonic region and intervals of $M_\infty = 0.1$ elsewhere. In these simulations the primary consideration was the position of the yaw CoP relative to the known CG position, and hence the static margin. Overall vehicle dynamics modelling had determined that the optimimum static margin (as a percentage of the vehicle wheel base) lay between 3% and 5% above $M_\infty = 0.5$. This was deemed to provide the optimum balance between directional stability and controllability and cross–wind sensitivity.

Table 3 shows the variation with Mach number of force coefficients, moment coefficients and corresponding static margin with the engine boundary conditions set to max throttle conditions at 2° yaw i.e. vehicle accelerating. Table 4 shows the variation with Mach number of force coefficients, moment coefficients and corresponding static margin with the jet engine boundary conditions set to idle and the rocket exhaust condition switched off at 2° yaw i.e. vehicle decelerating. The lift and drag coefficient variations with Mach number are shown graphically in Figure 10.

Comparison of Figures 9 and 10 indicate that the influence of a small yaw angle on the lift force and its distribution is negligible. Similar behaviour compared with design condition response is observed. The total lift increases through the subsonic and transonic regions, becoming positive as the vehicle reaches $M_\infty = 0.9$. However, the absolute total lift on the vehicle peaks at approximatly $M_\infty = 1.0$ at $0.92 \times 0.5 \times 1.2 \times 343 \times 343 \approx 20kN$ (slightly higher) assuming a free-stream density of $1.2kg/m^3$ and sound speed of $343m/s$.

Table 3 indicates that the maximum drag coefficient is $1.341m^2$ at $M_\infty = 1.1$ but drops back below the supersonic drag coefficient target of $1.3m^2$ by the time the vehicle reaches $M_\infty = 1.2$.

It is evident from Figure 11 that the vehicle's static margin tends to increase with Mach number. This is largely driven by the response of the shock system at the rear of the vehicle to small vehicle yaw angles resulting in a rearwards shift in the CoP. Also, there is significant shift in the CoP resulting from the transition from max throttle engine conditions to idle (and rocket off) engine conditions. The effect of reducing thrust, and in turn the strength of the jet eflux at the rear of the vehicle, is to reduce the static margin. Again, this is due to the complex shock system and downstream expansion at the rear of the vehicle along with the change in flow condition at the jet intake which controls the flow over the cockpit canopy. Also,

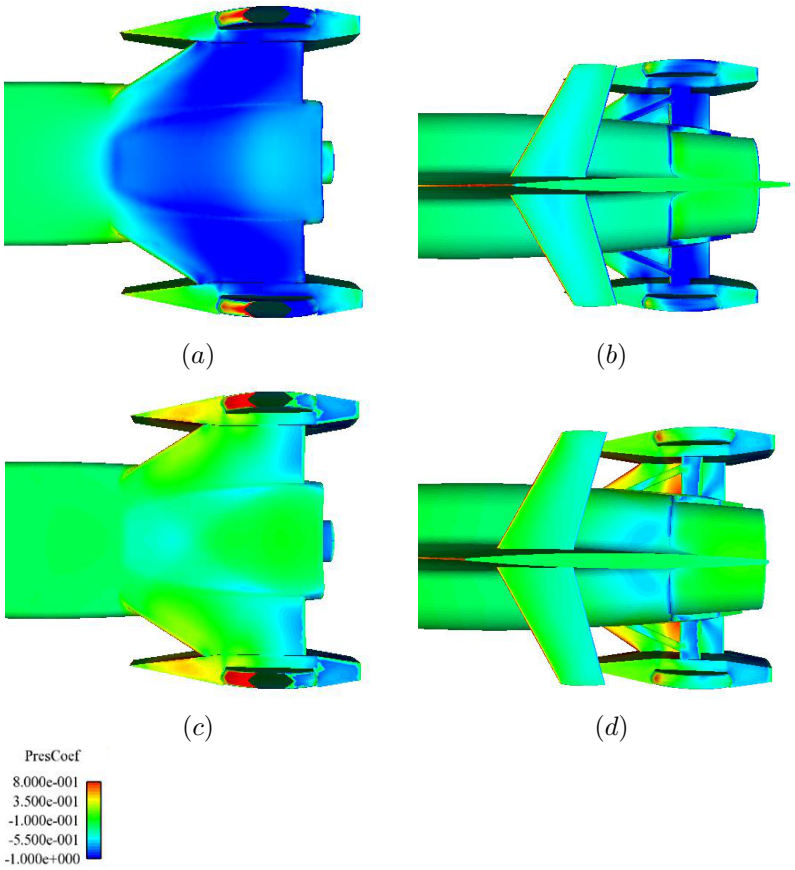

Fig. 8. Pressure coefficient distribution across external surfaces at rear:(a) underside $M_\infty = 0.5$; (b) top $M_\infty = 0.5$; (c) underside $M_\infty = 1.3$; (d) top $M_\infty = 1.3$

the rearward shift in CG position as the vehicle burns fuel leads to a reduction in static stability on deceleration. However, it is believed that the presence of air brakes during the deceleration phase will compensate for this. The CFD simulation work to confirm this will be completed as an ongoing investigation. Also note that the static margin is, for the most part, well above the 3% and 5% target. This is due to the fact that a series of directional stability studies at various stages in the design process indicated that static margin has an inescapable Mach number sensitivity with static margin increasing with Mach number. The fin has therefore been sized to ensure that the vehicle achieves the target in the worst case scenario of low speed (i.e. $M_\infty = 0.4$) with the inevitable consequence of higher than desired static margin values at high speed. This is a better situation, however, than the case of negative static margin over some of the Mach range.

9. Conclusions

This paper has outlined the process of predicting the aerodynamic characteristics of BLOODHOUND SSC using computational fluid dynamics. This is the process that has been used to guide the aerodynamic design (external shape) of BLOODHOUND SSC from initial concept to final design over a period of approximately 5 years. It should be noted that, even though the vehicle design is now frozen, this study is ongoing with an ever increasing databank of simulated vehicle behaviour being developed to be used as a benchmark for vehicle testing which is due to being in 2014. Also, the aerodynamic design process has not gone on in isolation from the development of other aspects of the vehicle design. Many of the critical design decisions on the vehicle have been compromises, balancing the requirements of the vehicle's dynamic performance, structure, control systems and engine interfaces.

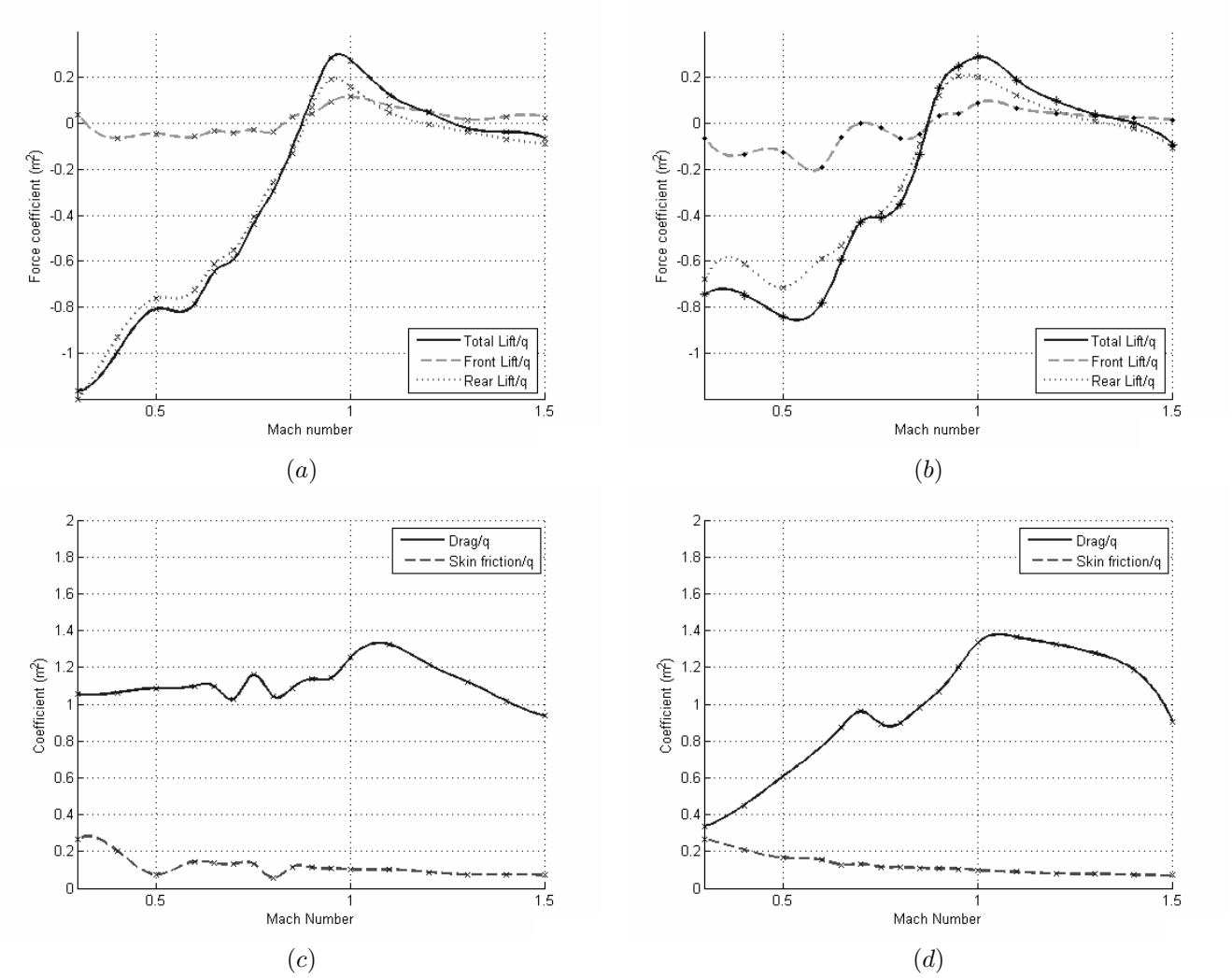

Fig. 9. Aerodynamic performance characteristics 0° yaw for config12 design, showing the lift distribution for:(a) maximum thrust conditions; (b) idle engine conditions as well as corresponding drag coefficients for :(c) maximum thrust conditions; (d) idle engine conditions

The aerodynamic characteristics of the final vehicle shape detailed in this paper indicate that the BLOODHOUND SSC vehicle is aerodynamically capable of safely achieving its target objective of a 1,000 mph Land Speed Record. The lift coefficient variation with Mach number is relatively benign and any variations that do exist can be safely 'trimmed' using the vehicle's front and rear winglets. The drag variation with Mach number is such that the thrust delivered from the EJ200 jet engine and rocket system are sufficient to propel it to its target speed and decelerate within the 12 mile Hakskeen Pan track. The vehicle is also predicted to be directionally stable with the yaw static margin remaining positive throughout the critical range between $M_{\infty} = 0.4$ and $M_{\infty} = 1.5$.

The CFD predictions detailed in this paper have been used in the overall vehicle performance model to produce the predicted 1,000 mph run profile shown in Figure 12. Note that the vehicle performance model includes a drag penalty due to the dust entrainment that will be present in the flow field, particularly at high speed when the shock waves are likely to break up the desert surface. This drag penalty has been calculated based on empirical data from the Thrust SSC vehicle testing.

	Mach Number	Front Wheel Lift/q (m^2)	Rear Wheel Lift/q (m^2)	Drag/q (m^2)	Lateral Force/q (m^2)	Lateral Moment /q (m^3)	Yaw CoP (m)	Accelerating CG Position (m)	Accelerating Static Margin (%)	Roll Moment/q (m^3)
subsonic	0.30	-0.747	-2.909	1.091	3.667	0.080	-0.022	-0.315	2.732	3.315
	0.40	-0.381	-1.876	1.097	2.432	-0.190	0.181	-0.315	5.013	2.573
	0.50	-0.015	-0.843	1.188	1.197	-0.460	0.384	-0.315	7.293	1.830
	0.60	-0.059	-0.727	1.134	1.201	-0.517	0.430	-0.315	7.814	1.840
	0.65	-0.019	-0.618	1.114	1.226	-0.575	0.469	-0.315	8.245	1.874
	0.70	-0.044	-0.553	1.063	1.224	-0.616	0.503	-0.315	8.634	1.882
	0.75	0.040	-0.485	1.102	1.270	-0.724	0.571	-0.315	9.388	1.943
transonic	0.80	0.002	-0.373	1.040	1.274	-0.748	0.587	-0.295	9.577	1.942
	0.85	0.040	-0.130	1.123	1.303	-0.899	0.690	-0.275	10.734	1.990
	0.90	0.052	0.086	1.176	1.362	-1.187	0.871	-0.255	12.767	2.097
	0.95	0.105	0.198	1.182	1.377	-1.232	0.895	-0.235	13.033	2.186
	1.00	0.127	0.165	1.293	1.357	-1.150	0.848	-0.215	12.504	2.151
	1.10	0.089	0.075	1.341	1.339	-1.268	0.947	-0.195	13.616	2.146
supersonic	1.20	0.063	0.002	1.255	1.263	-1.116	0.884	-0.195	12.911	1.974
	1.30	0.048	-0.044	1.145	1.193	-0.908	0.761	-0.175	11.533	1.867
	1.40	0.040	-0.066	1.049	1.157	-0.836	0.722	-0.175	11.084	1.808
	1.50	0.032	-0.088	0.952	1.122	-0.765	0.682	-0.175	10.636	1.750

Table 3. Characteristics under maximum thrust conditions with 2° yaw - Acceleration

Mach Number	Front Wheel Lift/q (m^2)	Rear Wheel Lift/q (m^2)	Drag/q (m^2)	Lateral Force/q (m^2)	Lateral Moment /q (m^3)	Yaw CoP (m)	Decelerating CG Position (m)	Decelerating Static Margin (%)
0.30	-0.050	-0.663	1.015	3.601	0.080	0.240	-0.175	5.675
0.50	-0.133	-0.723	0.903	1.190	-0.450	0.167	-0.175	4.859
0.65	-0.064	-0.535	0.873	1.222	-0.560	0.074	-0.175	3.805
0.80	-0.067	-0.284	0.894	1.269	-0.718	0.135	-0.175	4.500
0.95	0.059	0.222	1.168	1.367	-1.212	0.146	-0.175	4.622
1.10	0.072	0.141	1.345	1.301	-1.268	0.266	-0.175	5.972
1.30	0.051	0.066	1.230	1.193	-0.902	0.267	-0.175	5.979
1.50	0.017	-0.048	1.084	1.120	-0.760	0.287	-0.175	6.198

Table 4. Characteristics under idle thrust conditions with 2° yaw - Deceleration

The work detailed in the paper is ongoing and future CFD testing will be conducted to assess other off–design vehicle sensitivities such as ride–height sensitivity and the impact of the airbrake system being deployed on its directional stability. A series of unsteady simulations will also be carried out in order to determine the unsteady response of the vehicle, particularly in conditions such as deceleration with airbrakes deployed. It is also evident that there are still questions to be answered regarding the accuracy of the model, such as exactly how the shock waves will interact with the ground surface at Hakskeen Pan, particularly if the shock waves cause the surface to break up. This will require refinement of the CFD model in parallel with the testing of the vehicle. It is also planned to introduce a particle entrainment model into the simulation following the initial vehicle testing in 2014.

Acknowledgements

The authors gratefully acknowledge the financial support provided for this work by the U.K. Engineering and Physical Sciences Research Council (EPSRC) through their Grant EP/F032617 and Intel and HPC Wales for computational support.

References

[1] R. Noble, Thrust, Transworld, London, 1998.

[2] The Story of ThrustSSC, Corgi Books, London, 1998.

[3] K. Morgan, O. Hassan, N. P. Weatherill, Why didn't the supersonic car fly?, Mathematics Today, Institute of Mathematics and Applications, 35:110, 1999.

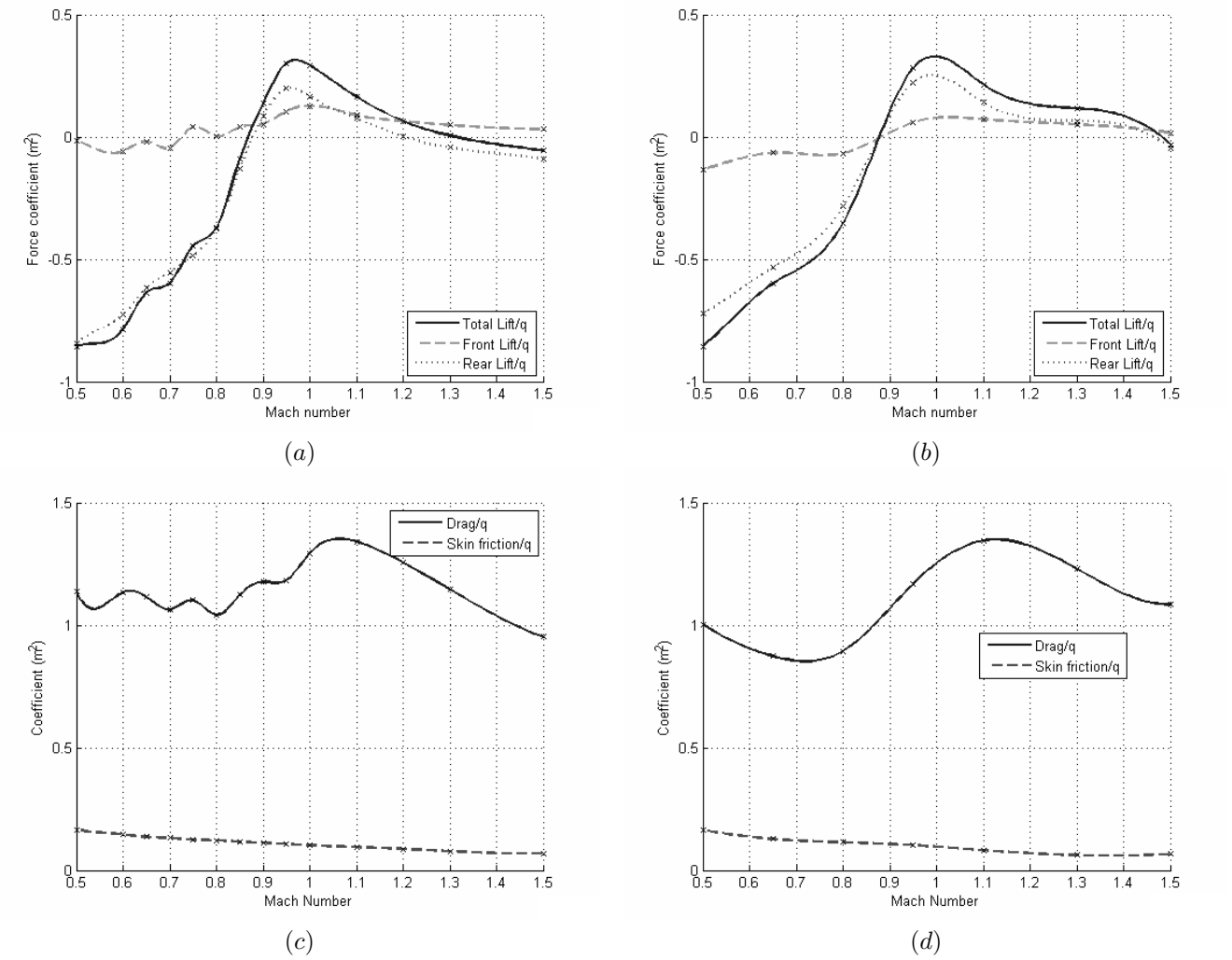

Fig. 10. Aerodynamic performance characteristics 2° yaw for config12 design, showing the lift distribution for:(a) maximum thrust conditions; (b) idle engine conditions as well as corresponding drag coefficients for :(c) maximum thrust conditions; (d) idle engine conditions

[4] K. Morgan, J. Peraire, J. Peiró and O. Hassan, The computation of 3–dimensional flows using unstructured grids, Computer Methods in Applied Mechanics and Engineering, 87:335–352, 1991.

[5] K. A. Sørensen, O. Hassan, K. Morgan and N. P. Weatherill. A multigrid accelerated hybrid unstructured mesh method for 3D compressible turbulent flow. Computational Mechanics 31, 101–114, (2003).

[6] J. Peraire, K. Morgan, and J. Peiró, Unstructured finite element mesh generation and adaptive procedures for CFD, Proceedings No: 464—Applications of Mesh Generation to Complex 3D Configurations, AGARD, Paris, 18.1–18.12, 1990.

[7] J. Peiró, J. Peraire and K. Morgan, FELISA system reference manual. Part 1–basic theory, University of Wales, Swansea Report C/R/821/94, 1994.

[8] O. Hassan, K. Morgan, E. J. Probert and J. Peraire, Unstructured tetrahedral mesh generation for three–dimensional viscous flows, International Journal for Numerical Methods in Engineering 39:549–567, 1996.

[9] N. P. Weatherill and O. Hassan, Efficient three–dimensional Delaunay triangulation with automatic boundary point creation and imposed boundary constraints, International Journal for Numerical Methods in Engineering 37:2005–2039, 1994.

[10] A. Harten, P. D. Lax, and B. van Leer, On upstreaming differencing and Godunov–type schemes for hyperbolic conservation laws, SIAM

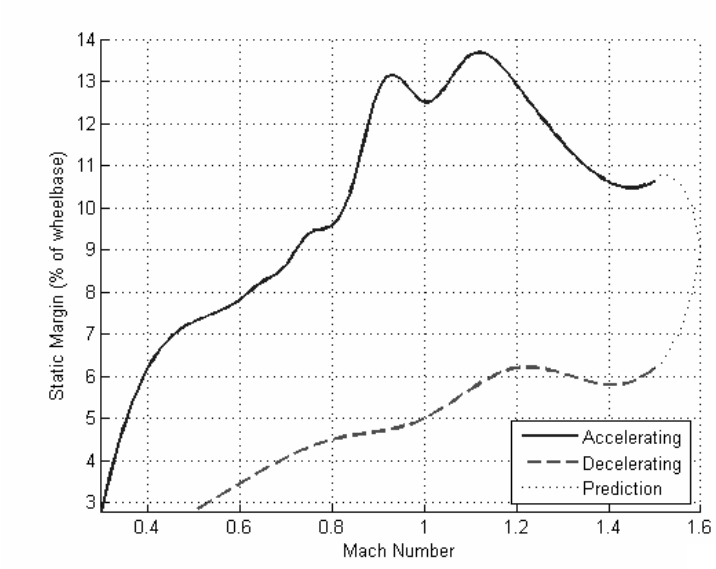

Fig. 11. Static margin as percentage of wheel base (yaw = 2°)

Revue, 25:35, 1983.

[11] P. Batten, N. Clarke, C. Lambert, D. M. Causon, On the choice of wavespeeds for the HLLC Riemann solver, SIAM Journal of Scientific Computation 18:1553–1570, 1997.

[12] D.C. Wilcox, Turbulence Modeling for CFD, DWC Industries Inc, La Canada, California, 2006.

[13] F. R Menter and Y. Egorov, A scale–adaptive simulation model using two–equation models, AIAA Paper 2055–1095, 2005.

[14] F. R. Menter, Review of the shear–stress transport turbulence model experience from an industrial perspective, International Journal of Computational Fluid Dynamics 23:305–316, 2009.

[15] B. J. Evans et al, Computational Fluid Dynamics Applied to the Aerodynamic Design of a Land–Based Supersonic Vehicle, Numerical Methods for Partial Differential Equations 27:141–159, 2011 (MAFELAP 2009 Special Issue).

[16] W. J. Usab, E. M. Murman, Embedded mesh solutions of the Euler equations using a multiple–grid method, in W. G. Habashi (editor), Advances in Computational Transonics, Pineridge Press, Swansea, 447–472, 1985.

[17] J.D. Anderson, Fundamentals of aerodynamics, McGraw–Hill, New York, 2001.

[18] P. R. Spalart and C. L. Rumsey, Effective inflow conditions for turbulence models in aerodynamic calculations, AIAA Journal, 45:2544âŁ“-2553, 2007.

[19] G. Karypis, V. Kumar, METIS4.0: Unstructured graph partitioning and sparse and sparse matrix ordering system. Technical report, Department of Computer Science, University of Minnesota (1998), http://www.cs.unn.edu/ metis

[20] A. Jameson, J.C. Vassberg, Computational Fluid Dynamics: Its Current and Future Impact, AIAA Paper 2001-0538, 2001.

[21] Nocedal, J. and S. J. Wright. Numerical Optimization, Second Edition. Springer Series in Operations Research, Springer Verlag, 2006

[22] B. Evans et al, Design optimisation using computational fluid dynamics applied to a land–based supersonic vehicle, the BLOODHOUND SSC, Structural and Multidisciplinary Optimisation, 24 July 2012, pp 1–16.

[23] R.A. Fisher, The Design of Experiments, Oliver and Boyd, Edinburgh (1935)

[24] T.P.Torda and T. A. Morel, Aerodynamic design of a land speed record car, Journal of Aircraft, 8:1029âŁ“-1033, 1971.

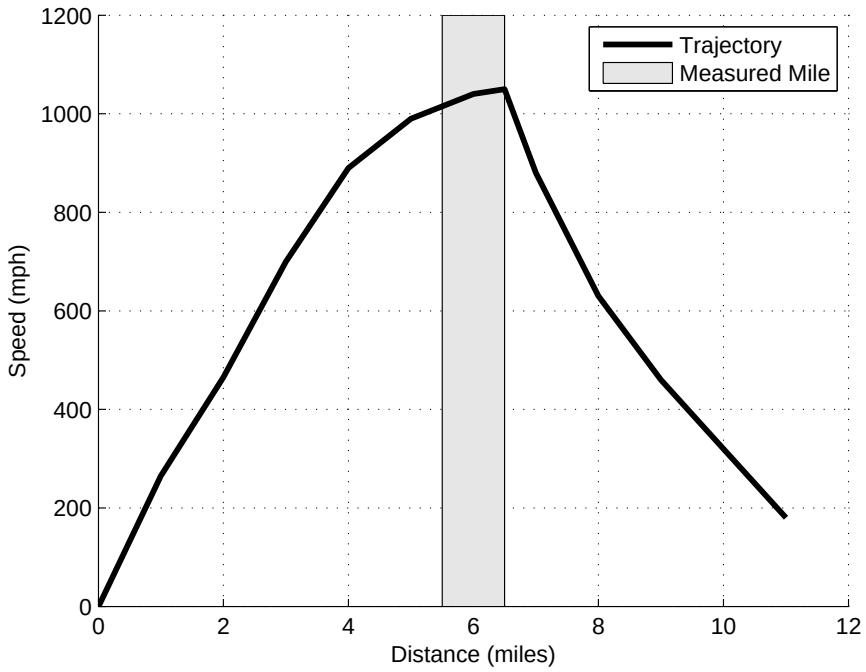

Fig. 12. Predicted path of BLOODHOUND SSC